Galerkin equivalent sources method for sound field reconstruction around diffracting bodies

Joannès Chambon, Jérôme Antoni, Simon Bouley

Galerkin Equivalent Sources Method for sound field reconstruction around diffracting bodies

Joannès Chambon,[1, a)] Jérôme Antoni,[1] and Simon Bouley.[2]
[1)] *Univ Lyon, INSA Lyon, LVA, 25 bis av. Jean Capelle F-69621, Villeurbanne Cedex, France.*
[2)] *MicrodB, 28 Chemin du Petit Bois, F-69134, Écully Cedex, France.*

(Dated: 3 October 2022)

The rising interest for three-dimensional acoustic imaging requires the improvement of the numerical models describing the propagation between a radiating body and a microphone array. The commonly used free field transfer functions boil down to assume a full acoustic transparency of the radiating object, which in some case may lead to misleading outcomes for their characterization. Among other approaches, Equivalent Sources Methods (ESM) emerged as a convenient and powerful approach to simulate scattered sound fields. In the following paper, an acoustic imaging algorithm named Galerkin ESM where equivalent sources are tailored to concomitantly match with microphone pressures and a Neumann boundary condition is proposed. By means of a projected matrix inversion and a backpropagation of the equivalent sources, Galerkin ESM aims at the direct synthesis of the pressure field around a diffracting body by making the most of an array measurement. This method is compared with two other existing imaging algorithms fueled by both free field and computed transfer functions. The impact of the chosen transfer model is discussed, and Galerkin ESM performances are evaluated on both numerical and experimental test cases.

[https://doi.org(DOI number)]

[XYZ] Pages: 1–15

I. INTRODUCTION

Acoustic propagation models that account for rigid body diffraction can be obtained with a wide range of numerical methods. When it comes to problems of infinite extent, the Boundary Element Method (BEM) emerges as the main option for its strong theoretical foundation and its convenience (see for instance Bonnet (1999) or Burton and Miller (1971) for an overview). As it got enhanced over the years to tackle its non-uniqueness issues, BEM became a complete but more complex and time consuming algorithm that requires consequent computational resources. Over and above the implementation of the method itself, BEM also requires a fine mesh management expertise. The use of advanced iterative solvers (see Saad, 2003) or Fast Multipoles introduced by Rokhlin (1990) led to significant speed ups, but at the same time turned BEM into a rather hard to master option.

With a view to provide a more simple and flexible alternative for more simple test cases, Koopmann *et al.* (1989) designed and assessed an Equivalent Sources Method (ESM). Its physical principle can be stated concisely: considering a rigid body exposed to an incident acoustic field, a volume interior distribution of elementary sources can be set to offset the boundary condition induced by the incident field on the skin of the object. The main interest of having equivalent sources strictly in the interior domain is to avoid numerical singularities issues encountered with BEM. These sources are thus considered as *acoustically equivalent* to the presence of the rigid body, and can be propagated toward the domain outside the skin to get the scattered sound field. After describing the theoretical background of ESM, Koopmann *et al.* (1989) also established its numerical version in which the rigid body and the volume of equivalent sources are respectively modeled by a rudimentary mesh and a discrete set of acoustic monopoles. Since then, ESM has been extensively studied and Lee (2017) proposed a review article where the key parameters of its proper implementation are identified:

- The optimal number equivalent sources was initially discussed by Koopmann and Fahnline (1991) on a cylindrical test case. Later on, Dunn and Tinetti (2004) experimentally showed that a ratio of three times less sources than nodes on the mesh provided the best results on practical cases.

- Their spatial distribution proved out to be directly linked to the conditioning of ESM matrices. Notably, a slight distinction was pointed out by Leblanc *et al.* (2010) between ESM with regularly distributed equivalent sources (Method of Fundamental Solutions, see Chen, 2006; Kondapalli *et al.*, 1992) and ESM using randomly located sources (Wave Superposition Method, see again Koopmann *et al.*, 1989). They showed that the first is a well-posed problem but suffers from non-uniqueness issues at particular frequencies while the latter is

[a)] Also at MicrodB. Author to whom correspondence should be addressed. Electronic mail : joannes.chambon@microdb.fr

more robust but prone to ill-conditioning deficiencies. This can be dealt with using singular value regularization (see Lee *et al.*, 2011). Pavić (2005) also designed a time consuming but accurate algorithm to determine optimised spatial configurations.

- Their retreat distance toward the skin of the rigid body is also a key driver for the proper functioning of ESM approaches. The stake is comparable to BEM collocation techniques : equivalent sources far from the mesh struggle to precisely match with complex incident acoustic fields while sources close to the skin are likely to be numerically unstable because of singularities. Bai *et al.* (2011) recently tackled this issue and proposed leads to find the optimal balance.

- Lastly the nature of the equivalent sources plays a role in the efficiency of the method. ESM can be described in terms of single and double layer potentials (see Wilton *et al.*, 1993), and Jeans and Mathews (1992) first investigated the use of dipolar equivalent sources, while Ochmann (1995) later on suggested that any type of sources (like spherical harmonics, see Bouchet *et al.*, 2000) could be used.

Featuring all these refinements (see Lee, 2017, for a more in-depth review), ESM is a relevant alternative to BEM for its straightforward implementation and its accuracy on a large scope of test cases.

Bearing in mind the advantages cited above, ESM naturally got introduced into acoustic imaging methods over the last years. The generic set-up common to all acoustic imaging problems,

$$\mathbf{p} = \mathbf{H}\mathbf{q}, \tag{1}$$

where a source grid $\mathbf{q}$ has to be identified from microphonic pressures $\mathbf{p}$ and a collection of acoustic Frequency Response Functions (FRF) $\mathbf{H}$, can be cast in ESM problems: it aims at identifying a set of sources acoustically equivalent to those that actually produced the sound field covered by the microphone array. When it comes to acoustic imaging, the ESM terminology was used for instance by Fernandez-Grande *et al.* (2017); Hald (2020); Sarkissian (2005); Valdivia and Williams (2007) for applications in near-field acoustic holography, by Leclère *et al.* (2017) for inverse methods or Pereira *et al.* (2015, chapter 2) for imaging in enclosed space. If they differ in the algorithm used to identify the sources, the common ground to all these references lies in their use of a discrete set of equivalent monopoles (or dipoles, see for example Valdivia, 2018) to reconstruct a radiated acoustic field from array measurements. However, another common aspect is that they no more involve these equivalent sources in the simulation of a particular boundary condition in contrast to the historical purpose of ESM.

A few tries to align the use of equivalent sources in acoustic imaging with scattering simulation are to be mentioned : Le Magueresse (2016, section 6.2.4) first introduced the idea of using Koopman's ESM to fill the $\mathbf{H}$ matrix in Eq.(1) with coefficients taking into account the diffracting behaviours in the acoustic scene. Later on, Le Magueresse *et al.* (2020, section 4) also highlighted how the use of such transfer functions can matter to avoid misleading interpretations of source identification on an experimental engine test bench. At the same time, Chambon *et al.* (2020) used the same approach in a wind tunnel, and showed how ESM could be used for aeroacoustic source identification on a car mirror to improve beamforming maps resolution.

Drawing on this, the connection between Koopman's ESM approach and acoustic imaging remained to be formalized, which is the point addressed in this article. The concept of fitting a set of equivalent sources to conform to a given boundary condition is borrowed from ESM, and included in the acoustic imaging inverse problem. Considering a Neumann boundary condition, this embedding takes the form of an orthogonal projection of the equivalent sources on the kernel of a matrix modeling the impedance of a rigid body. The basic inverse problem in Eq.(1) remains, but finds itself restricted to solutions satisfying an orthogonality constraint similar to those stemming from Galerkin methods. The aim of such an approach is also a crossover between classical ESM and acoustic imaging : the data provided by the phased microphone array is processed to identify virtual equivalent sources, and the latter are to be propagated to synthesize the acoustic fields at areas of interest.

The proposed algorithm, hence named Galerkin ESM, is depicted in this paper. Section II is dedicated to its mathematical formulation, from the statement of the inverse problem to the backpropagation step providing the display of the pressure maps synthesized from equivalent sources. Then, in section III, the emphasis is put on an in-depth study of the orthogonal projector involved in Galerkin ESM. A lead to precondition the kernel matrix with a physical maximization of the radiation efficiency of the sources is exposed. In section IV, Galerkin ESM is put to the test head-to-head against the well-assessed acoustic imaging methods that are Conventional Beamforming (CBF) and iterative Bayesian Focusing (iBF) on a various set of test cases featuring scattered sound propagations. With a full control on the target pressure fields, this benchmark is an opportunity to discuss the importance of supplying imaging algorithms with realistic transfer functions instead of the commonly used free field models. The last section consists in an illustrative application of Galerkin ESM on an academical experimental set of measurements.

Conventions and notations

Throughout this article, vectors are represented by bold lowercase letters and matrices by bold uppercase letters. $\mathbf{M}^{\mathsf{H}}$ denotes the transpose conjugate of a complex matrix, and $\mathbf{M}^{+}$ stands for its Moore Penrose inverse. The orthogonal complement of a given Hilbert space $\mathcal{H}$

is noted as $\mathcal{H}^{\perp}$. The complementary of a given set $\mathcal{E}$ is $\bar{\mathcal{E}}$. The euclidean norm of a vector $\mathbf{v}$ is written $\|\mathbf{v}\|$ and its p-norm $\|\mathbf{v}\|_p$. The column space of a matrix $\mathbf{M}$ is noted as Im $\mathbf{M}$ and its kernel as $\ker \mathbf{M}$.

Lastly, the convention chosen for phase sign is $\mathrm{e}^{-\mathrm{i}\omega t}$.

II. GALERKIN ESM

A. Overall methodology

First is considered a three-dimensional radiating body bounded by a closed surface Γ. The acoustic field is sensed via a set of M microphones located at the positions $(\mathbf{r}_i)_{i\leq M}$. The purpose of the method is to provide a description of the exterior acoustic field (both phase and amplitude) at a given pulsation ω by means of equivalent sources placed inside Γ. The latter are to be determined with respect to the measured pressures $p(\mathbf{r}_i)_{i\leq M}$ on the one hand, and to the impedance condition induced by the behaviour of the body on the other hand.

A discrete formulation of the problem is proposed now. Γ is modeled by a surfacic mesh featuring N nodes of positions $(\mathbf{r}_j)_{j\leq N}$ and a set of N_s equivalent monopolar acoustic sources are introduced at the positions $(\mathbf{r}_k)_{k\leq N_s}$ in the volume Ω.

Let $\mathbf{G}\in\mathbb{C}^{M\times N_s}$ be the matrix defining the acoustic free-field transfer functions between the equivalent sources and the pressure at the microphone positions, i.e. $\forall i\leq M,\ \forall l\leq N_s$,

$$\mathbf{G}_{il}=-\mathrm{i}\omega\rho\frac{\mathrm{e}^{\mathrm{i}k\|\mathbf{r}_i-\mathbf{r}_l\|}}{4\pi\|\mathbf{r}_i-\mathbf{r}_l\|},\quad \mathbf{r}_i\in\bar{\Omega},\mathbf{r}_l\in\Omega. \tag{2}$$

Similarly can be defined the matrix $\mathbf{G}_\Gamma\in\mathbb{C}^{N\times N_s}$ describing the source to pressure transfer between the equivalent sources and the nodes on Γ, and $\mathbf{T}_\Gamma\in\mathbb{C}^{N\times N_s}$ the source to normal velocity transfer $\forall j\leq N,\ \forall l\leq N_s$,

$$\mathbf{T}_{\Gamma,jl}=\frac{\mathrm{e}^{\mathrm{i}k\|\mathbf{r}_j-\mathbf{r}_l\|}}{4\pi\|\mathbf{r}_j-\mathbf{r}_l\|}\left(1-\mathrm{i}k\|\mathbf{r}_j-\mathbf{r}_l\|\right)\cos\theta_{jl},\quad \mathbf{r}_j\in\Gamma,\mathbf{r}_j\in\Omega. \tag{3}$$

where θ_{jl} denotes the angle between $\mathbf{r}_j-\mathbf{r}_l$ and the direction normal to Γ at $\mathbf{r}_j$.

Finally the impedance imposed by the radiating body is introduced as $\left(z_j=\frac{p(\mathbf{r}_j)}{v_n(\mathbf{r}_j)},\mathbf{r}_j\in\Gamma\right)_{j\leq N}$.

After stacking the M pressures $p(\mathbf{r}_i)$, the N_s equivalent sources flow $q(\mathbf{r}_l)$, and the impedances z_j into the column vectors $\mathbf{p}$, $\mathbf{c}$ and the diagonal matrix $\mathbf{Z}$ respectively, the inverse problem under scrutiny boils down to

$$\begin{cases}\mathbf{p}=\mathbf{G}\mathbf{c} & \text{(measurements matching)}\\ (\mathbf{Z}\mathbf{T}_\Gamma-\mathbf{G}_\Gamma)\,\mathbf{c}=0 & \text{(boundary condition).}\end{cases} \tag{4}$$

From a mathematical standpoint, the goal here will be to solve a classical acoustic imaging inverse problem whose solution has to be projected on a null space accounting for the presence of the boundary condition.

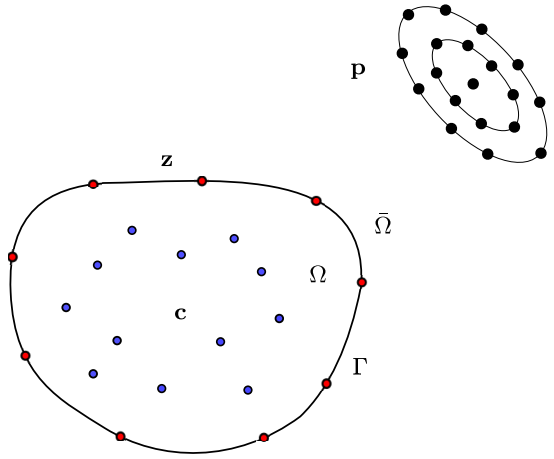

FIG. 1. (Color online) A set of equivalent monopolar sources with complex amplitudes $\mathbf{c}$ (blue dots) is sought after to match both the impedance condition $\mathbf{z}$ on the skin of the body and the pressure $\mathbf{p}$ measured by a microphone array at a given frequency.

Assuming Eq.(4) solved, the last step of the approach consists in the repropagation of the obtained sources $\mathbf{c}$ on any observation region Γ_{obs} thanks to free field transfer matrices defined similarly to Eq.(2) and (3).

In this paper, the particular case of a perfectly rigid body is investigated for the sake of simplicity. In other words, the admittance on Γ is set to zero which implies

$$\mathbf{T}_\Gamma\mathbf{c}=0 \tag{5}$$

to account for a Neumann boundary condition, and the overall problem as stated in Eq.(4) becomes

$$\begin{cases}\mathbf{p} &= \mathbf{G}\mathbf{c} & \text{(measurements adequation)}\\ \mathbf{T}_\Gamma\mathbf{c} &= 0 & \text{(boundary condition).}\end{cases} \tag{6}$$

B. $\mathbf{T}_\Gamma$ Null space

As the acoustic inverse problem turns into an algebraic projected inversion, the settings of the operating matrices dimensions is a major stake for the practical implementation of the method.

M and N are considered as inputs of the problem: the number of microphones is given by the available hardware, and the number of nodes describing the body is fixed in accordance with the minimum wavelength under scrutiny. Concerning the test cases presented in this paper, a 5 nodes per wavelength condition is matched to ensure a margin (Lee *et al.* (2011) showed that ESM approaches could be more resilient than FEM/BEM on this point).

The number of equivalent sources N_s is a key parameter of the method and requires further clarification. As

it is mandatory that Eq.(5) admits non zero solutions for the proper operation of the method, the lowest N_s is first given by the rank theorem:

$$N_s = \mathrm{Rank}\left(\mathbf{T}_\Gamma\right) + \dim\left(\ker \mathbf{T}_\Gamma\right). \tag{7}$$

As $\mathbf{T}_\Gamma$ *is of full rank* (i.e. $\mathrm{Rank}\left(\mathbf{T}_\Gamma\right) = \min\left(N, N_s\right)$), a non-empty kernel implies $N_s > N$ and the number of equivalent sources must be greater than the number of nodes supporting the boundary condition on the body.

Under this assumption, the resolution of Eq.(4) involves the extraction of the kernel of $\mathbf{T}_\Gamma$. The simplest way to do so is based on the classical relationship

$$\ker \mathbf{T}_\Gamma = \left(\mathrm{Im}\mathbf{T}_\Gamma^{\mathsf{H}}\right)^{\perp}. \tag{8}$$

From then on, the QR decomposition (see for example Golub and Van Loan, 1996) of $\mathbf{T}_\Gamma^{\mathsf{H}}$ is sufficient to sample a K sized matrix $\mathbf{B} \in \mathbb{C}^{N_s \times K}$ from the null space of $\mathbf{T}_\Gamma$. Let us first introduce

$$\begin{aligned}\mathbf{T}_\Gamma^{\mathsf{H}} &= \mathbf{QR} \\ &= \underbrace{\begin{bmatrix} \mathbf{Q}_{1,1} & \cdots & \mathbf{Q}_{1,N} & \mathbf{Q}_{1,N+1} & \cdots & \mathbf{Q}_{1,N_s} \\ \mathbf{Q}_{2,1} & \cdots & \mathbf{Q}_{2,N} & \mathbf{Q}_{2,N+1} & \cdots & \mathbf{Q}_{2,N_s} \\ \vdots & \cdots & \vdots & \vdots & \cdots & \vdots \\ \mathbf{Q}_{N_s,1} & \cdots & \mathbf{Q}_{N_s,N} & \mathbf{Q}_{N_s,N+1} & \cdots & \mathbf{Q}_{N_s,N_s} \end{bmatrix}}_{\mathrm{Im}\mathbf{T}_\Gamma^{\mathsf{H}} \quad \text{null space of } \mathbf{T}_\Gamma} \mathbf{R},\end{aligned} \tag{9}$$

where $\mathbf{Q} \in \mathbb{C}^{N_s \times N_s}$ is an unitary matrix and $\mathbf{R} \in \mathbb{C}^{N_s \times N}$ is an upper triangular matrix.

Equation (9) can be rewritten as

$$\mathbf{T}_\Gamma^{\mathsf{H}} = \begin{bmatrix} \mathbf{Q}_1 & \mathbf{Q}_2 \end{bmatrix} \mathbf{R}, \tag{10}$$

with $\mathbf{Q}_1 \in \mathbb{C}^{N_s \times \mathrm{Rank}(\mathbf{T}_\Gamma)}$ describing the image of $\mathbf{T}_\Gamma^{\mathsf{H}}$ and $\mathbf{Q}_2 \in \mathbb{C}^{N_s \times (N_s - \mathrm{Rank}(\mathbf{T}_\Gamma))}$ being a set of orthogonal rows in the kernel of $\mathbf{T}_\Gamma$. From there, any matrix $\mathbf{B}$ of the form

$$\mathbf{B} = \mathbf{Q}_2 \mathbf{\Lambda}, \quad \mathbf{\Lambda} \in \mathbb{C}^{(N_s - \mathrm{Rank}(\mathbf{T}_\Gamma)) \times K} \tag{11}$$

ensures that $\mathbf{T}_\Gamma \mathbf{B}$ will equal zero.

The $\mathbf{B}$ matrix is the cornerstone of the proposed Galerkin ESM as it plays two major roles:

- Because of its similarity with $\mathbf{Q}_2$, it can force equivalent sources to respect the Neumann boundary condition stated in Eq.(5).
- The appropriate construction of $\mathbf{\Lambda}$ allows the reduction of the the inverse problem dimension in Eq.(4) from N_s to K unknowns.

Leads to define what can be a relevant definition of this matrix is investigated in section III.

C. Practical inversion

The initial system (4) can now be reduced to a single inverse problem

$$\mathbf{p} = \mathbf{Gc} = \mathbf{GBd} \tag{12}$$

where the new unknown vector $\mathbf{d} \in \mathbb{C}^K$ may be understood as a set of equivalent source coefficients in a basis accounting for the Neumann boundary condition on the body.

Since it is desirable for this new statement of the problem to be correctly conditioned, a parametric condition arises from Eq.(12) as it should not be underdetermined. This means that the size of the kernel basis K has to be larger than the output dimension M of the matrix $\mathbf{GB}$ to invert, which necessarily leads to

$$M \leq K \leq N_s - N. \tag{13}$$

This prerequisite on the number of equivalent sources will be supported by numerical considerations in section IV.

Now that the inverse problem boils down to the formulation Eq.(12) remains the choice of an inversion algorithm to reach the solution $\mathbf{d}$. A large scope of sophisticated algorithms are available in the literature, (see for example Leclère *et al.* (2017) or Merino-Martínez *et al.* (2019) for a review). The shape of the optimal solution $\mathbf{d}$ (i.e. for example sparse or with minimum energy) is case-dependant and likely to be influenced by the choice of $\mathbf{\Lambda}$. For that reason, the generic choice would be to make use of an L^2 regularized inversion. This is the one made in the framework of this article in the validation sections, with the regularization parameter set up according to Pereira *et al.* (2015) Bayesian regularization algorithm.

Once $\mathbf{c}$ is recovered from Eq.(12), the last step consists in the backpropagation of the optimal equivalent sources vector $\hat{\mathbf{c}} = \mathbf{B}\hat{\mathbf{d}}$ to estimate the radiated pressure in the region of interest within $\bar{\Omega}$. This is simply achieved with the free field propagator following

$$\mathbf{p}_{\mathrm{obs}} = \mathbf{G}_{\bar{\Omega}} \hat{\mathbf{c}}. \tag{14}$$

For this backpropagation to be meaningful, a noticeable precaution has to be highlighted: since the equivalent sources arising from Galerkin ESM are designed to acoustically model the object defined by Γ, it is mandatory for this region of interest not to intersect Γ. This would indeed boil down to evaluating the pressure radiated by the body inside or on itself, and most likely lead to incoherent results and interpretations. Indeed, like classical ESM or BEM, the Galerkin inverse problem is dedicated to the simulation of the acoustic field outside the source region since the $1/r$ singularity of the monopoles is unmanageable within Ω. Apart from this area, it is supposed to provide a realistic synthesized acoustic field outside the rigid body based on the microphone array measurements.

In the end, the overall execution of Galerkin ESM is summarized in Algorithm 1.

ALGORITHM 1: Step-by-step description of Galerkin ESM

Require: Array measures $\mathbf{p} \in \mathbb{C}^M$, N node positions on Γ, N_s equivalent sources positions in Ω, and a region of backpropagation Γ_{obs} featuring N_{obs} points.
Ensure: $M \leq N_s - N$ and $\Gamma \cap \Gamma_{\text{obs}} = \varnothing$
$\mathbf{G} \in \mathbb{C}^{M \times N_s} \leftarrow$ Eq.(2).
$\mathbf{T}_\Gamma \in \mathbb{C}^{N \times N_s} \leftarrow$ Eq.(3).
$\mathbf{Q}_2, \mathbf{R} \leftarrow$ QR decomposition of $\mathbf{T}_\Gamma^{\mathsf{H}}$.
$\mathbf{\Lambda} \in \mathbb{C}^{(N_s - \text{Rank}(\mathbf{T}_\Gamma)) \times K} \leftarrow$ User defined, see section III.
$\mathbf{B} \leftarrow \mathbf{Q}_2 \mathbf{\Lambda}$.
$\hat{\mathbf{d}} \leftarrow$ regularized inversion of $\mathbf{p} = \mathbf{GBd}$.
$\mathbf{p}_{\text{obs}} \leftarrow \mathbf{G}_{\Gamma_{\text{obs}}} \mathbf{B} \hat{\mathbf{d}}$.

From the computational cost point of view, the two most significant steps are the QR decomposition ($\mathcal{O}\left(N^3\right)$ operations using `numpy` Householder reflectors) and the inversion of $\mathbf{GB}$ that will depend on $\mathbf{\Lambda}$ and the chosen inverse methods.

III. KERNEL LAYOUT THROUGH PRINCIPAL SURFACES

When choosing the simplest form for $\mathbf{\Lambda}$, i.e. a rectangular matrix with unitary entries on its diagonal, there is no genuine reason to expect any dimension reduction from $N_s - N$ to K: in that case $\mathbf{B}$ is directly sampled from the QR decomposition, which is a pure mathematical operation with no physical meaning involved. The selection of columns from $\mathbf{Q}_2$ is thus bound to be arbitrary and it is shown in the next section that Galerkin ESM is unlikely to provide meaningful results with small values of K in this set up.

As mentioned in the previous section, the construction of $\mathbf{\Lambda}$ thus deserves an in-depth analysis since it impacts both the physical meaning of the equivalent sources model and the numerical cost of the inverse problem. The current section is dedicated to a practical way to define an acoustic operator from which are derived principal radiating surfaces. For the sake of clarity, only one promising option is advocated in this section, but some other leads could be studied as well depending on the application cases.

Sources with maximum radiation efficiency

The proposed option is to *tidy up* the columns of $\mathbf{Q}_2$ following an order of increasing efficiency in terms of acoustic radiated power. For that purpose, the choice was to test Galerkin ESM featuring a $\mathbf{\Lambda}$ matrix filled with K eigenvectors associated to the largest eigenvalues of the radiation efficiency operator.

Given a closed surface completely covering the rigid body ($\Gamma_W \subset \bar{\Omega}$) and discretized in N_W nodes and surface elements, the acoustic power propagated by the equivalent sources $\mathbf{c}$ through Γ_W is determined by

$$W = \frac{1}{2}\Re e\left(\mathbf{v}_n^{\mathsf{H}} \mathbf{A} \mathbf{p}\right) = \frac{1}{2}\Re e\left(\left(\mathbf{T}_{\Gamma_W}\mathbf{c}\right)^{\mathsf{H}} \mathbf{A} \mathbf{G}_{\Gamma_w}\mathbf{c}\right) \quad (15)$$

where $\mathbf{T}_{\Gamma_W}, \mathbf{G}_{\Gamma_W}$ are the free field propagation matrices of $\mathbf{c}$ on Γ_W respectively for normal velocity and pressure, and $\mathbf{A} \in \mathbb{R}^{N_W \times N_W}$ is a diagonal matrix containing the areas of Γ_W surface elements.

From that perspective, it seems relevant to favour distributions of equivalent sources with the best radiation efficiency when reducing the size of the inverse problem. In practice this can be achieved by setting the columns of $\mathbf{\Lambda}$ as

$$\mathbf{\Lambda} = [\boldsymbol{\lambda}_1, \ldots, \boldsymbol{\lambda}_K] \quad (16)$$

where

$$\boldsymbol{\lambda}_i = \underset{\substack{\|\mathbf{u}\|=1 \\ \mathbf{u}^{\mathsf{H}}\boldsymbol{\lambda}_j=0,\ j\leq i-1}}{\arg\max} \frac{1}{2}\mathbf{u}^{\mathsf{H}}\Re e\left(\mathbf{Q}_2^{\mathsf{H}}\mathbf{T}_{\Gamma_W}^{\mathsf{H}}\mathbf{A}\mathbf{G}_{\Gamma_w}\mathbf{Q}_2\right)\mathbf{u}. \quad (17)$$

All in all, the matrix $\mathbf{B} = \mathbf{Q}_2\mathbf{\Lambda}$ brings in a combination of a projection on the kernel of $\mathbf{T}_\Gamma$ while sorting the equivalent sources distribution in ascending order regarding their radiation efficiency on Γ_W. Through this intermediary step, a physical behaviour is coupled to $\mathbf{Q}_2$ and allows to significantly reduce the size of the inverse problem without damaging its accuracy. An illustration of how radiate such principal surfaces and the quantitative gain of the introduction of $\mathbf{\Lambda}$ defined with Eq.(17) is put forth in section IV E.

Another subsidiary benefit lies in the orthogonality between the columns of $\mathbf{B}$. Considering further applications of Galerkin ESM, one could think of decomposing the overall radiated acoustic power on the principal surfaces according to

$$W = \sum_{i=1}^{K} w_i, \quad \text{where } w_i = \left|\hat{d}_i\right|^2 \Pi_i, \quad (18)$$

with Π_i being the i^{th} eigenvector of the matrix $\frac{1}{2}\Re e\left(\mathbf{Q}_2^{\mathsf{H}}\mathbf{T}_{\Gamma_W}^{\mathsf{H}}\mathbf{A}\mathbf{G}_{\Gamma_w}\mathbf{Q}_2\right)$ in Eq.(17) and $\hat{d}_i$ the i^{th} coefficient of $\hat{\mathbf{d}}$. Such a process is likely to provide some insightful hierarchy in the operating radiative patterns (see Fig. 6,7,8 in the next section for a example on an academic case).

IV. NUMERICAL VALIDATION

A comparison of Galerkin ESM with other popular acoustic imaging algorithms is proposed in this section. The purpose of the method is to reconstruct acoustic fields outside a rigid surface. To evaluate these methods from that angle, a spherical geometry is chosen: with respect to Fig. 1, Γ is modeled here by a spherical mesh of radius $a = 0.3$ meters featuring 1280 triangular elements and $N = 642$ nodes. As they get equally spread over the sphere, this set of nodes allows a 5 elements per wavelength condition up to $ka = 15$.

A. Spherical Related Transfer Functions

The acoustic field radiated around a rigid box (see for example Bouchet *et al.*, 2000; Koopmann *et al.*, 1989) is a common test case for ESM approaches. However, the point of this paper is also to put Galerkin ESM to the test in terms of three-dimensional diffracted source identification based on array imaging. From that perspective, the spherical case offers valuable advantages. First of all, the pressure in the vicinity of a rigid sphere given a monopolar source on its skin is analytically known (Williams (1999, section 8.8)): using the notations of Eq.(2) and considering the sphere centered on the origin, the acoustic transfer function between a unitary monopolar source located at $\mathbf{r}_l$ on the spherical surface Γ and a microphone at $\mathbf{r}_i$ in the outer field is given by

$$\mathbf{H}^{\mathrm{s}}_{il} = \frac{-\mathrm{i}\rho c}{4\pi a^2}\sum_{n\in\mathbb{N}}(2n+1)\frac{h_n(k\,\|\mathbf{r}_i\|)}{h'_n(ka)}P_n\left(\frac{\mathbf{r}_i\cdot\mathbf{r}_l}{\|\mathbf{r}_i\|\,\|\mathbf{r}_l\|}\right), \tag{19}$$

where h_n, h'_n and P_n respectively refers to spherical Bessel Functions of second kind and order n, its derivative, and Legendre polynomials of order n. Duda and Martens (1998) even proposed an accelerated routine to compute high orders of formulation (19), and Pereira (2013, chapter 2) empirically linked the maximum order $n_{\max}$ to the frequency of interest through

$$n_{\max} > 1.2(ka)^2 + 8\frac{r/a+1}{r/a} \tag{20}$$

to ensure a truncation error lesser than 10^{-9} on the sum. Equation (19) provides the acoustic field resulting from any combination of monopoles on the surface of the sphere, and thus allows to assess Galerkin ESM on monopolar source identification.

An observation surface Γ_{obs} is set up for the display of the acoustic fields propagated by the equivalent sources from Galerkin ESM and the sources identified through classical acoustic imaging methods. It consists in an additional sphere of radius $a_{\mathrm{obs}} = \frac{4}{3}a$ merged with a cutting plane of size $5a$ (see Fig. 2). This set-up allows to check discrepancies between the obtained propagated fields and the analytical one on both near and far field.

For the sake of simplicity, the choice was made to use a regular spherical array of radius $\frac{16}{3}a$ with $M = 250$ microphones.

B. Acoustic imaging methods

For each validation case below, Galerkin ESM is benchmarked against two already existing acoustic imaging approaches.

The first one is Conventional Beamforming (CBF) (see Chiariotti, 2019). Known to be fast and robust, CBF is theoretically justified for the identification of a single monopolar radiating source in a free field toward the array. Even if its relevance may be questioned given the more complex radiation patterns used here, it remains

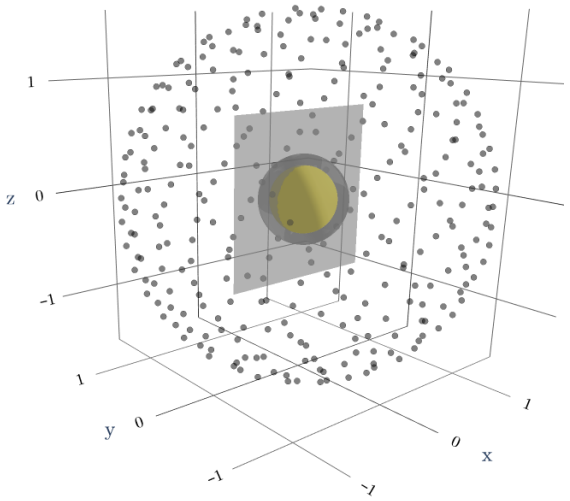

FIG. 2. (Color online) Geometrical set-up for validation. The yellow surface is the control point support Γ, the transparent grey is Γ_{obs} and the cloud of points around it is the microphone array.

a reference in industrial applications and a comparison with CBF output is a necessary step for the evaluation of new acoustic imaging methods. If $\mathbf{H} \in \mathbb{C}^{M\times N}$ denotes the acoustic transfer matrix between the nodes on Γ and the array, either free field or more refined depending on what is numerically available, CBF aims at identifying sources energies on Γ throughout

$$\forall j \leq N, \quad |q_j|^2 = \frac{\mathbf{e}_j^{\mathsf{H}}\mathbf{H}^{\mathsf{H}}\mathbf{p}\mathbf{p}^{\mathsf{H}}\mathbf{H}\mathbf{e}_j}{\|\mathbf{H}\mathbf{e}_j\|^4}, \tag{21}$$

with $\mathbf{e}_j \in \mathbb{C}^N$ being the j^{th} element of the canonical basis.

The second method is iterative Bayesian Focusing (iBF), a current state-of the-art algorithm initially proposed by Antoni (2012). The full description of this algorithm as used in the scope of this article is to be found in Antoni *et al.* (2019, Algorithm 1), featuring a generalized multivariate complex Gaussian as prior density function. iBF was assessed as an imaging approach that provides the full cross spectral matrix of the sources, and includes a regularization step to deal with noisy measurements or poorly conditioned FRFs.

In the end, the comparison study features five different approaches to reconstruct the acoustic field:

1. CBF between N monopole sources on the mesh Γ and the array, featuring the free-field propagation of Eq.(2) in the transfer matrix $\mathbf{H}$ of Eq.(21).

2. CBF involving the analytical transfer Eq.(19) in $\mathbf{H}$.

   With these first two is tested the usability of CBF for sound field synthesis and its ability to handle non free-field FRFs.

3. iBF between N monopole sources on Γ and the array, with free-field FRF and without any prior hypothesis on the sources in terms of regularization.

   This one serves at evaluating what a *turnkey* version of iBF produces.

4. Galerkin ESM as described in section II, with $N_s = 3N = 1926$ and $K = N_s - N = 1284$ in a first stage, to maintain a margin regarding Eq.(13). No principal surfaces for the validation in comparison with other imaging algorithms to remain general. The equivalent sources are distributed inside the mesh according to classical ESM literature guidelines : half of it are placed on a 85% scaled replica of Γ and the other half randomly located but at least $0.15a$ m away from the control points (see Leblanc *et al.*, 2010).

5. Lastly iBF again, but with the use of the analytical FRF in $\mathbf{H}$ and a strong sparsity constraint (L^1 regularization). It should be noted that this last approach differs from the first four as it is the only one that features a suitable a priori on the sources. It aims at displaying the maximum degree of accuracy reachable on the reconstructed scattered field when the inverse method perfectly fits with the ground truth source distribution.

The aim of such a methodology is multiple:

- Checking the error induced by approximated FRFs in CBF and iBF when the actual propagation is not free field.
- Assessing the ability of CBF and iBF to benefit from the use of a perfectly accurate transfer function.
- Evaluating Galerkin ESM comparatively to what is reachable with *blind* acoustic imaging approaches (i.e. without proper assumptions on the source distribution) and with the perfectly tuned iBF version.

C. Uncorrelated monopolar sources

The first test case consists in the reconstruction of the acoustic field produced by $N_{\text{src}} = 10$ uncorrelated monopoles randomly placed on the yellow sphere (on Fig. 2). The cross spectral matrix (CSM) resulting from their combined radiation at the microphones is computed through

$$\mathbf{S_{pp}} = \mathbf{H}^{\text{s}}\mathbf{S_{qq}}\left(\mathbf{H}^{\text{s}}\right)^{\text{H}}, \tag{22}$$

where $\mathbf{H}^{\text{s}}$ is determined according to Eq.(19) and $\mathbf{S_{qq}}$ is set to the identity matrix in order to describe completely uncorrelated sources of unitary strength.

Each algorithm presented in sections II and IV B is then fed with this CSM and the sources obtained are finally backpropagated on a circle of radius $1.5a$. The directivities resulting from this process are plotted on Fig. 3.

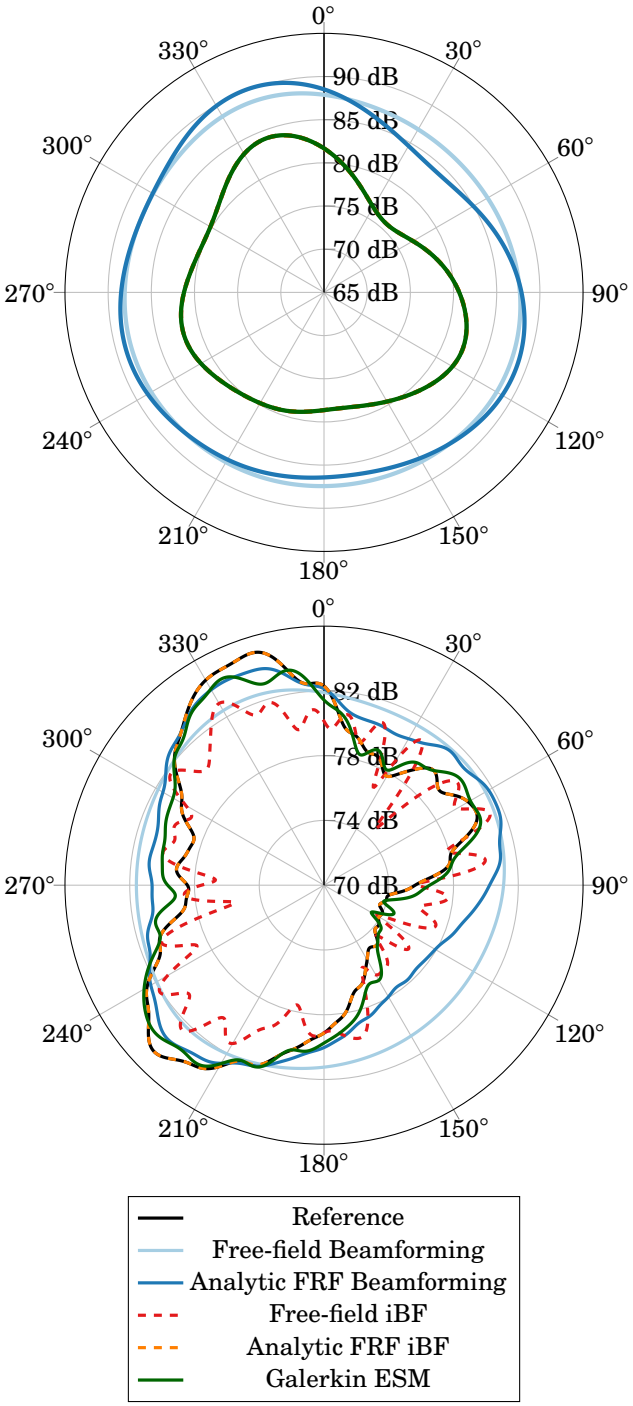

FIG. 3. (Color online) Directivity pattern of 10 uncorrelated monopoles on a rigid sphere at $ka = 1$ (top) and $ka = 13$ (bottom), computed through various imaging algorithms. At low frequency, both Galerkin ESM and iBF are matching with the reference (all 4 plots are overlapped).

This first configuration is supposed to fall in the range of all the methods assessed, but this first benchmark offers interesting preliminary conclusions. Methodwise, it seems that the overall directivity pattern is seized by both CBF, iBF and Galerkin ESM.

It appears then that the use of the accurate FRFs leads to an enhancement at high frequencies, dealing with some 5 dB discrepancies for both beamforming and Bayesian Focusing. This item is quite intuitive and shows how the diffraction of the spherical body plays a role in the acoustic transfer and should not be underestimated.

With respect to the classical methods, Galerkin ESM (green dotted line Fig. 3) may be ranked at the second place in terms of accuracy. It outperforms CBF in general, deals with the impact of diffraction in a much better way than iBF with free-field FRFs, but does not compete with the latter when used with spherical transfer functions and induced sparsity.

It may be noticed that at both high and low frequencies, iBF with correct transfer functions (yellow dashed line) perfectly managed to reconstruct the reference directivity of the ten sources. This basically means that the number and the disposition of the microphones allows enough information to fully describe the acoustic field. That being said, it should be concluded that Galerkin ESM is by far the best performing algorithm among the without *a priori* approaches even if there still are room for improvements.

D. Correlated monopolar sources

The panel of imaging approaches is now put to the test for the recovery of an acoustic field produced by the same ten monopoles, but this time correlated: the CSM and the the reference directivity pattern is obtained in the same way as in the previous section using Eq.(22), except that $\mathbf{S_{qq}}$ is no longer the identity matrix. Instead, it gets defined as

$$\mathbf{S_{qq}} = \mathbf{I}_{N_{\text{src}}} + \mathbf{\Delta}_{N_{\text{src}}} + \mathbf{\Delta}_{N_{\text{src}}}^{\text{H}} \tag{23}$$

where $\mathbf{\Delta}_{N_{\text{src}}}$ is an upper triangular matrix randomly filled with 0 or 1 entries. The ten sources on the sphere are thus either fully or not correlated one with each other, causing a much more complex and uneven directivity pattern than in the previous paragraph.

Results are plotted on Fig. 4. As expected, CBF loses relevance when dealing with correlated sources and fails at nailing the interference peaks. Regarding iBF, the scattering effect of the sphere becomes of first order at large ka number and the quality of the output is damaged as long as a free field transfer function is used. In that case, levels seem to be underestimated with respect to the reference: inherently to their propagation model, the identified sources are namely interferated *through* the spherical mesh at the backpropagation step of the process leading to overall lower levels because of the inappropriate L^2 regularization with respect to the source model.

Here again, Galerkin ESM does well as being in the efficiency range of the optimal set-up offered by iBF with spherical related transfer functions. Every interference lobe is well rendered at both high and low frequencies, only remain some local discrepancies with the reference. This uneven aspect may likely result from a non optimal disposition of the equivalent sources, which constitutes the major lead for further improvements of the method.

With a view to exemplify the potential applications of Galerkin ESM, the backpropagation depicted in Eq.(14) is achieved and displayed on Fig. 5 for correlated monopoles (5 only for the sake of readability). Comparing (a) and (b), this result highlights to what extent the free assumption leads to misleading interpretations on the left side of the sphere. On this test case, it appears that iBF with accurate FRFs and Galerkin ESM only can provide a reliable backpropagated sound field.

All in all, the conclusion regarding the numerical test cases seems consistent. In terms of methods ranking, it can be stated that :

- Beamforming is unusable at low frequencies for radiated field reconstruction. The poor spatial resolution on the identified sources leads to over smoothed propagated fields completely blurring directivity patterns. At large ka values, the use of accurate FRFs as steering vectors for CBF slightly improves it but this statement remains especially when dealing with correlated sources.

- At high frequencies, i.e. when the scattering behaviour of the sphere is of first order, the identification of the outer pressure field with iBF should be achieved with great precautions. Without any prior knowledge on the sources nature, the generic parametrization of the algorithm with free-field transfer functions and L^2 regularization leads to significant inaccuracies. In practice, this means that iBF should be used for array-based field synthesis only when refined transfer functions and funded assumptions on the sources are available.

- Galerkin stands out as a powerful alternative to have a proper simulation of the acoustic field around the rigid sphere without ground truth FRFs. Discrepancies with the reference are observable but local and acceptable. The peaks induced by the scattering presence of the sphere is well modeled by the kernel projection added to precondition the free-field transfer matrices as exposed in section II.

E. Principal Surfaces

Given its reasonable size, the spherical case used throughout this section is ideal to evaluate the contribution of principal surfaces introduced in section III.

A 5/4 scaled version of the mesh plotted in Fig. 2 was chosen as Γ_W discretized in $N_W = N = 642$ nodes. The $\mathbf{\Lambda}$ matrix of size $N_s \times N_s$ was filled with columns computed following Eq.(17) and it is insightful to visually check their radiative pattern as basis vector for the

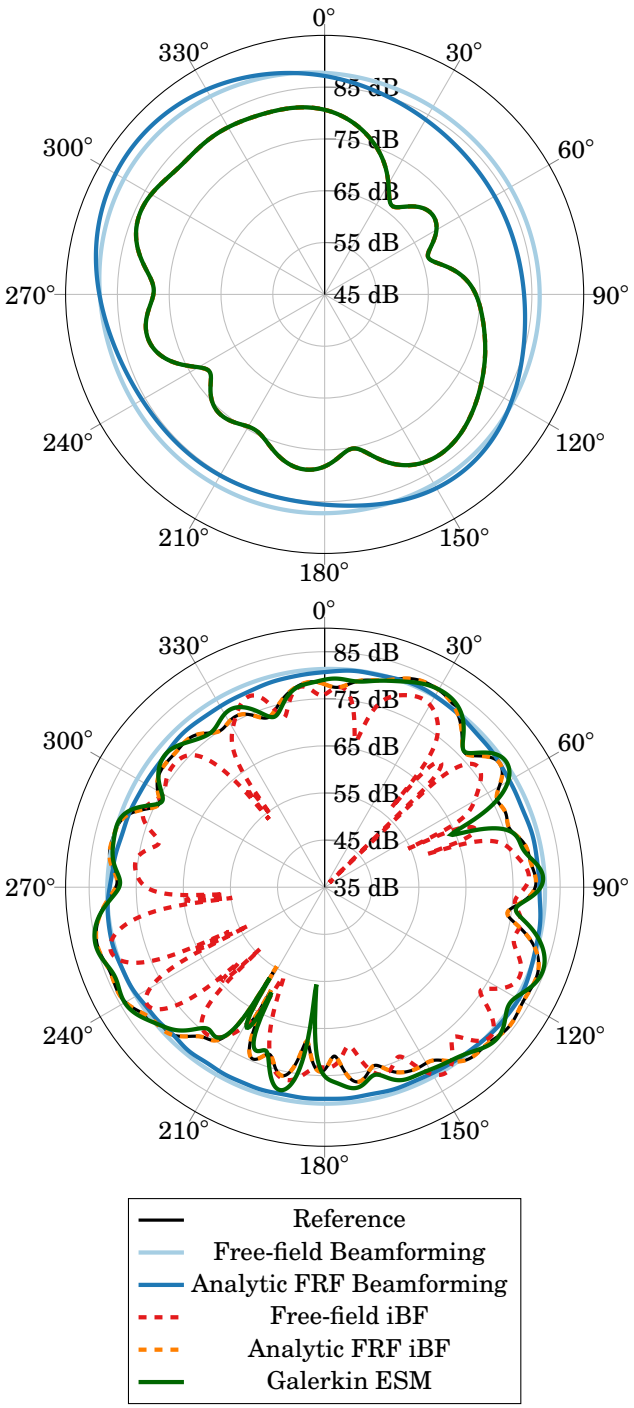

FIG. 4. (Color online) Directivity pattern of 10 correlated monopoles on a rigid sphere at $ka = 1$ (top) and $ka = 13$ (bottom), computed through various imaging algorithms. At low frequency, both Galerkin ESM and iBF are matching with the reference (all 4 plots are overlapped).

Galerkin ESM inverse problem. For that purpose, the amplitude of the pressure field radiated by the columns of $\mathbf{B}$ on Γ_{obs}, i.e.

$$\mathbf{p}_{\text{obs}}^{\boldsymbol{\lambda}_i} = \mathbf{G}_{\Gamma_{\text{obs}}}\mathbf{B}_i \tag{24}$$

was computed for various i values and displayed in Fig. 6 with $\boldsymbol{\Lambda}$ being the identity matrix and Fig. 7 with $\boldsymbol{\Lambda}$ issued from Eq.(17).

A relevant point arises from the observation of these figures and confirms the reasoning exposed in section IV E: On the one hand, in terms of acoustic radiation, no obvious hierarchy seems to sort the basis vector inside $\mathbf{B}$ when $\boldsymbol{\Lambda}$ is the identity. In other words, every columns of $\mathbf{Q}_2$ share the same radiation efficiency and it is unlikely to sample $K < N_s - N$ of them without any loss on the accuracy on the Galerkin ESM outcome.

On the other hand, from Fig. 7 it appears that the power-optimized version of $\boldsymbol{\Lambda}$ leads to much more workable basis functions, with a clear ranking between the most radiating vector at low i values and the weakest ones at larger indices.

The quantitative assessment of this interpretation was conducted and shown in Fig. 8. The latter exposes the global L^2 relative error on Γ_{obs} between the analytical pressure field and the one propagated by Galerkin ESM sources, with respect to the number of columns K selected from $\boldsymbol{\Lambda}$. Simultaneously is plotted the relative acoustic power of the equivalent sources integrated on Γ_W for rising truncation values K in the sum of Eq. (18).

It can be stated from this graph that the optimized formulation of $\boldsymbol{\Lambda}$ drastically improves the convergence speed of Galerkin ESM. On this particular test case for example, the -13 dB error ratio is obtained for $K \approx 0.8(N_s - N) = 1027$ when $\mathbf{B}$ is only sampled from $\mathbf{Q}_2$ while the same accuracy can be achieved with $K \approx 0.4(N_s - N) = 513$ with the power oriented version of $\boldsymbol{\Lambda}$. This earning represents a significant reduction of the dimension of the inverse problem in Eq.(12) for practical applications of the method.

The red lines assesses the point made above with Eq. (18): when Eq.(17) is used for the construction of $\boldsymbol{\Lambda}$, most of the acoustic energy is concentrated in the first coefficients of $\hat{\mathbf{d}}$ while at least 85% of them are required to reconstruct the same energy levels when $\boldsymbol{\Lambda}$ is simply the identity matrix.

F. Computational efficiency

Results above on the spherical test case were computed with Python 3.7 on an Intel Core I7 8750H (2.2 Ghz). Averaged on 25 runs of the code, 1.7 seconds per frequency were needed for the QR decomposition, 1.2 for the $\mathbf{B}\boldsymbol{\Lambda}$ calculation in Eq.(17) and 2.3 for the $\mathbf{GB}$ regularized inversion.

Given the results displayed in the current section, the fair comparison would be with iBF combined with realistic FRFs. Considering a generic test case, iBF itself is of the same complexity than the $\mathbf{GB}$ inversion but the FRF simulation has to achieved with FEM, BEM or

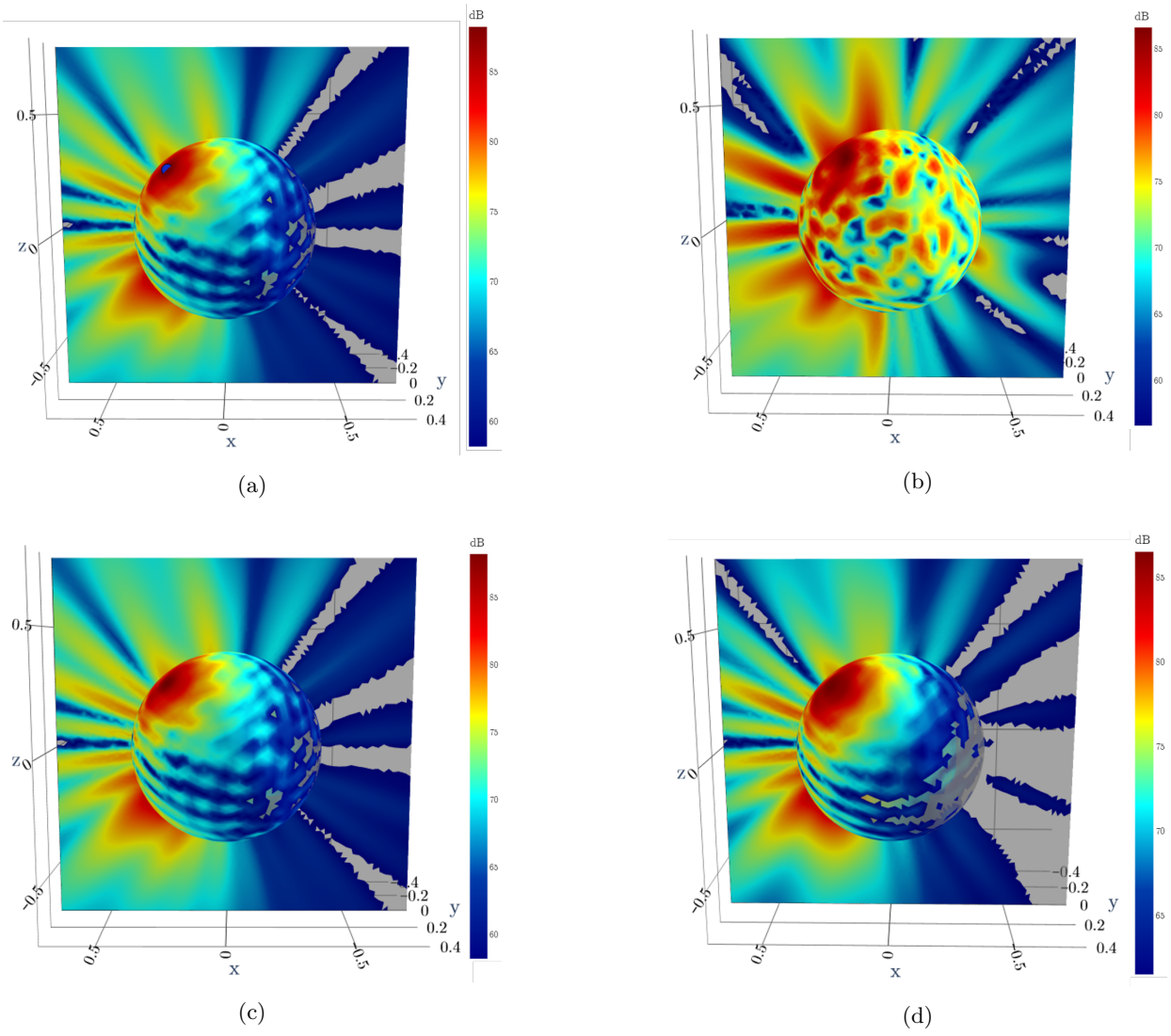

FIG. 5. (Color online) Acoustic pressure (amplitude) on Γ_{obs} radiated by 5 randomly correlated monopoles at $ka = 13$ (with a 20 dB dynamic range). (a) Analytical sound field. (b) Sound field propagated by sources identified with iBF featuring free-field FRF. (c) Sound field propagated by sources identified with iBF featuring analytical FRF. (d) Sound field propagated by sources identified with Galerkin ESM.

classical ESM and it is likely that in the end the overall performance does not overrun Galerkin ESM.

V. EXPERIMENTAL VALIDATION

This last section lays out an experimental validation of Galerkin ESM. The aim of this final point is to gauge the behaviour of the method dealing with actual microphone array measurements on a large frequency range. The chosen case is a wooden mock-up flush mounted with omnidirectional sources, as described on Fig. 9. The latter is modeled with triangular mesh of $N = 2377$ vertices.

Its characteristic length equals $L = 0.77$ meters, and the planar array features M = 36 analogical microphones placed at 12 centimetres from the sources plan. Similarly to what was proposed in section IV, sources A and C were fully correlated while the last one remained uncorrelated. The measurement is a 9.84 seconds record sampled at $f_s = 25600$ Hz.

The session took place in a semi anechoic room with a locally treated ground, and array signals were post processed using the Welch periodogram with a Hann window. The block size was set to 2560 samples with a 50% overlap to reach a 10 Hz frequency resolution up to 12800 Hz.

Since no analytical transfer function is available for such a geometry, the relevance of this last section namely lies in this transfer function computation step: whatever the choice of the numerical method (ESM, BEM, FEM, etc.), computing transfer functions involves numerical re-

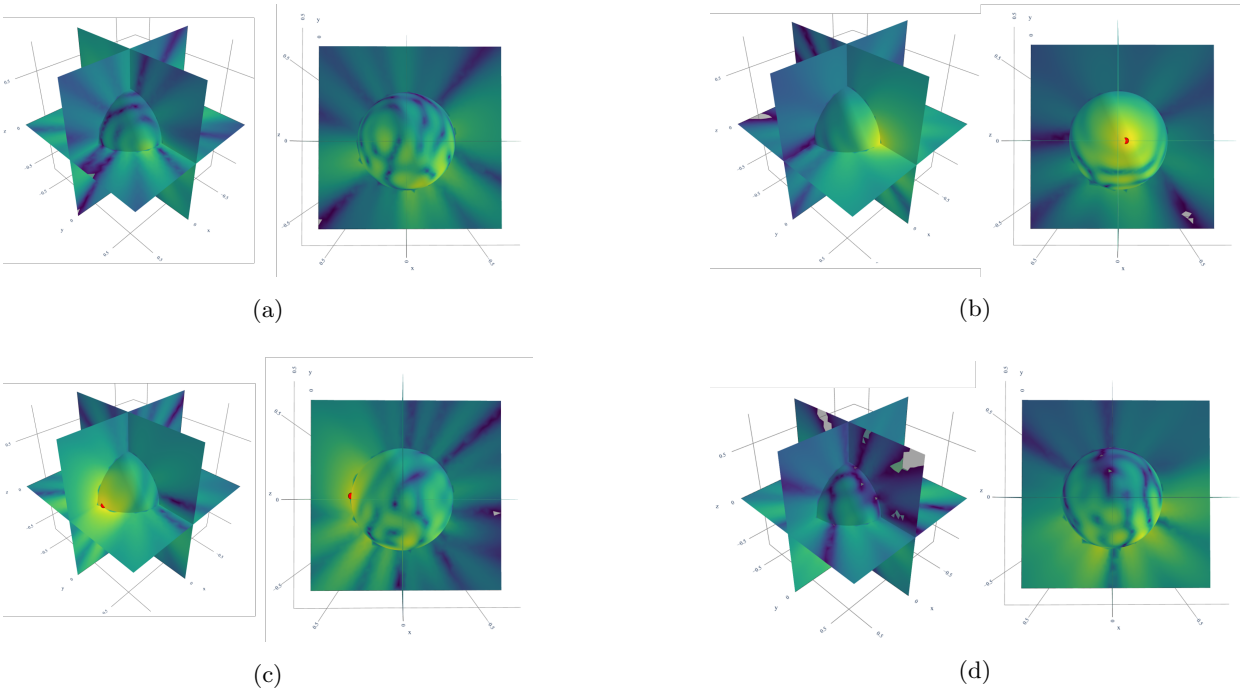

FIG. 6. (Color online) Pressure amplitudes on Γ_{obs} radiated by the i^{th} column of $\mathbf{Q}_2\mathbf{\Lambda}$ ($\mathbf{\Lambda}$ being the identity matrix). (a) $i = 1$, (b) $i = 10$, (c) $i = 100$, (d) $i = 250$ and $ka = 8.24$. Plots are displayed within a 30 dB dynamic range, and the red dot indicates the maximum level location.

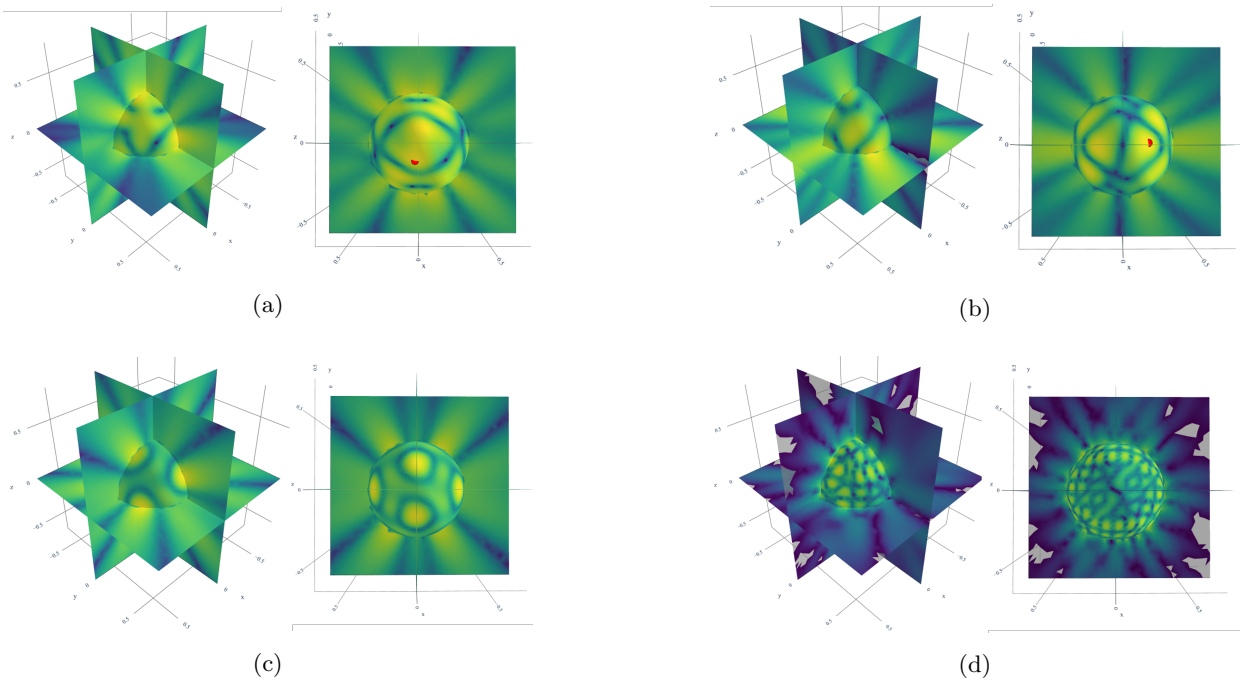

FIG. 7. (Color online) Pressure amplitudes on Γ_{obs} radiated by the i^{th} column of $\mathbf{Q}_2\mathbf{\Lambda}$ ($\mathbf{\Lambda}$ being defined by Eq.(17)). (a) $i = 1$, (b) $i = 10$, (c) $i = 100$, (d) $i = 250$ and $ka = 8.24$. Plots are displayed within a 30 dB dynamic range, and the red dot indicates the maximum level location.

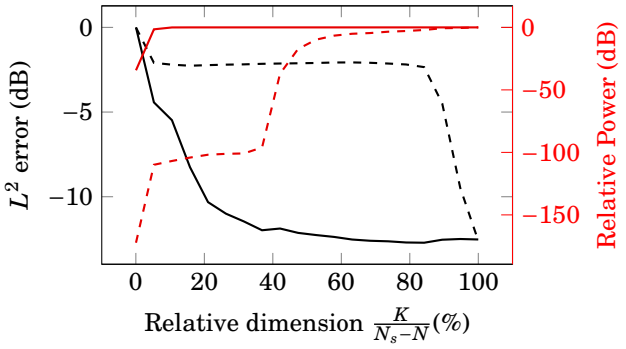

FIG. 8. (Color online) Reconstruction indicators for 10 correlated monopoles on a rigid sphere at $ka = 1$. In black is plotted the L^2 relative error, in red is displayed radiated power from Eq. (18). Dashed lines features $\mathbf{\Lambda} = \mathbf{I}$ while solid lines were obtained with $\mathbf{\Lambda}$ sampled from the radiation efficiency operator.

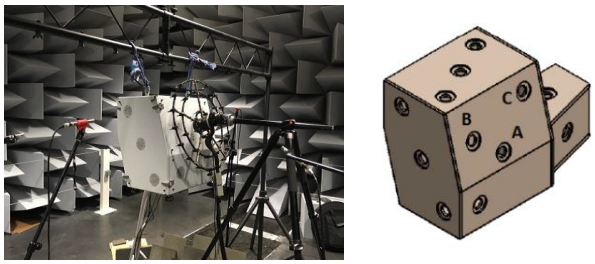

(a) (b)

FIG. 9. (Color online) Experimental set-up, from Le Magueresse *et al.* (2018). (a) Actual disposition of the array facing the source panel. (b) Disposition of the flesh mounted sources.

sources and may induce additional errors for complex meshes. The Galerkin ESM proposed in this paper could be seen as an alternative method that includes scattering effects in the model while bypassing this transfer simulation step.

With a view to recover the sound field propagated by the three sources around the engine, the same methods as in the previous section were applied here: CBF, iBF and Galerkin ESM, with the difference that this time only free field FRFs can be provided to the two first ones. The numerical modelisation of the set up is exposed on Fig. 10.

An illustrative display of the associated synthesized fields is given on Fig. 11, at a frequency at which scattering effects are likely to be significant (kL ratio far greater than one).

Preliminary observations of these acoustic maps are enlightening. As expected CBF is unsuitable to seize the acoustic produced by the correlated sources A and C. iBF and Galerkin ESM are in accordance on the side of the faces with the sources but differ on the part of Γ_{obs} with

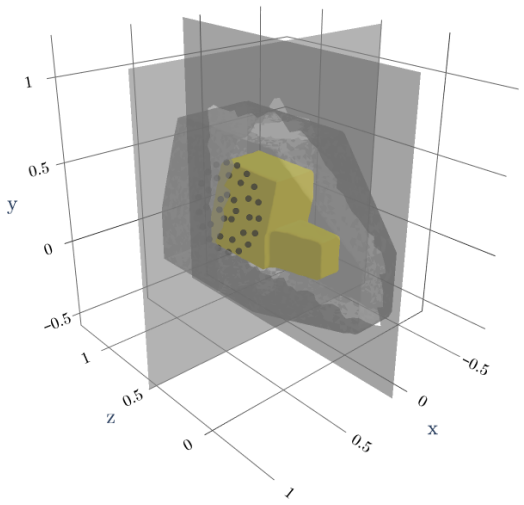

FIG. 10. (Color online) Numerical set-up for experimental set up. The yellow surface is the control point support Γ, the transparent grey is Γ_{obs} and the 36 black dots represent the microphone array placed at 12 cm from the mock-up.

pressure levels scattered around the mock-up. At first glance it seems that the acoustic shadow zones caused by the presence of the wooden structure find its most faithful depiction with the Galerkin ESM synthesized pressure field.

Another quantitative evaluation on the experimental case is displayed on Fig. 12. It exposes the back-propagated pressure level on reference microphone placed 12cm in the alignment behind the array shown on Fig. 9. For the sake of readability, the beamforming curve was post-processed by propagating only the three local maxima corresponding to the A, B and C points of the CBF map. At low ka numbers, Galerkin ESM all three methods yield a good adequation with the measured level, with a small edge for iBF and Galerkin ESM. However, beamforming rapidly tends to be globally inappropriate as frequency rises and iBF is subject to discrepancies at specific frequency ranges compared to Galerkin ESM. With regard to Fig. 11, this is consistent with the fact that acoustically masked areas in $\bar{\Omega}$ do differ between iBF and Galerkin ESM issued backpropagation because of the misleading free-field propagator. Lastly, this last plot gives a first empirical clue on the maximum frequency reachable with the chosen number of equivalent sources concerning our method (here approximately) 1800 Hz). As for classical ESM, a sensitivity study will be conducted in further studies to define more precise guidelines on that specific issue.

VI. CONCLUSION

Galerkin ESM is introduced as a promising algorithm to reproduce sound fields scattered around diffracting bodies from array measurements. The transcription of

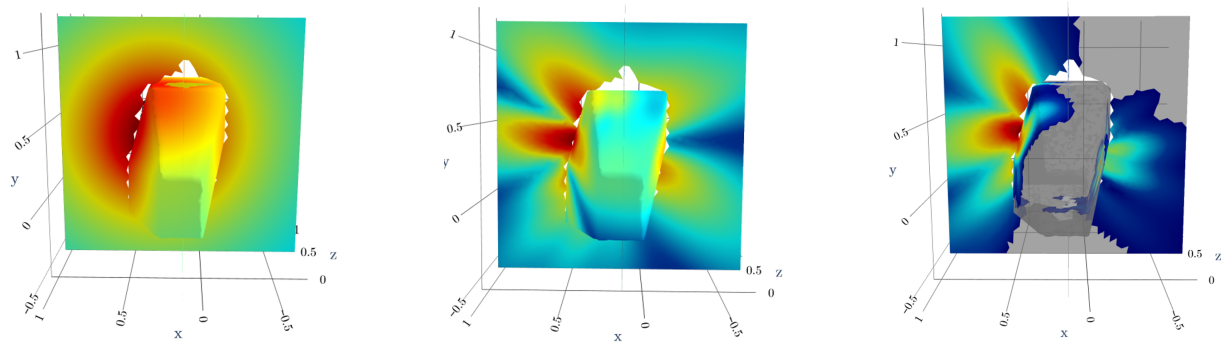

(a) (b) (c)

FIG. 11. (Color online) Acoustic pressure (amplitude) backpropagated on Γ_{obs} at $kL = 21$ (relative levels with a 30 dB dynamic range). (a) Sound field propagated by sources identified with CBF featuring free field FRF. (b) Sound field propagated by sources identified with iBF featuring free field FRF. (c) Sound field propagated by sources identified with Galerkin ESM.

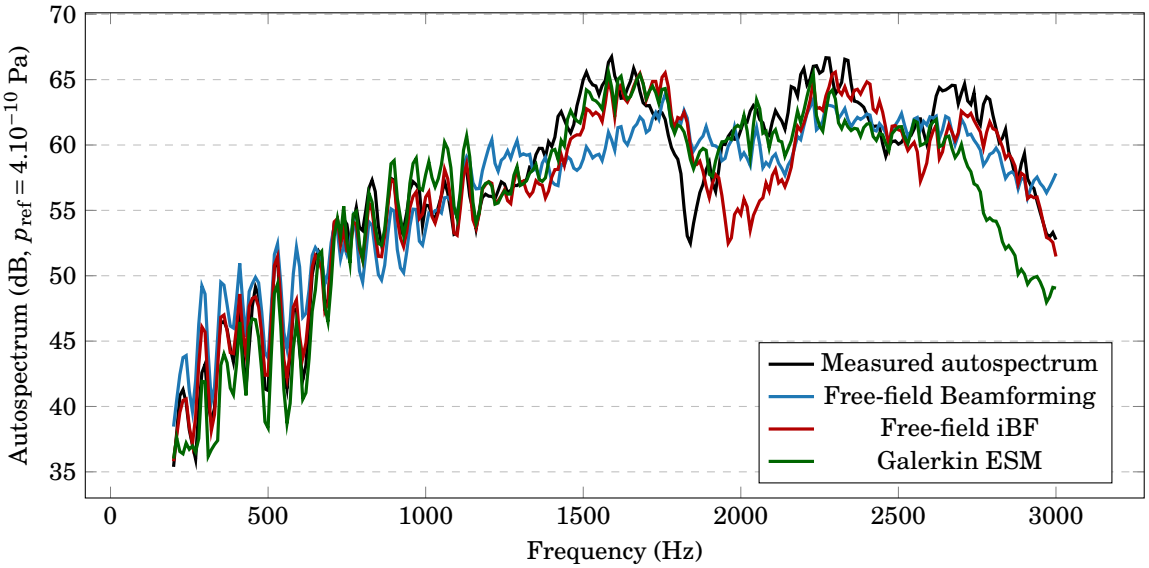

FIG. 12. (Color online) Backpropagated levels on the $kL = 2.8$ to 48.6 frequency range.

a Neumann boundary condition as a matrix kernel inclusion is fully described, and integrated to the acoustic imaging inverse problem. A sub-process dedicated to the reordering of the kernel is also proposed to reduce the dimension of the resulting inverse problem, by maximizing the overall radiation efficiency the equivalent sources.

The method is assessed first on numerical data issued from correlated and uncorrelated monopoles flush mounted on a rigid sphere. Since highly realistic FRF can be analytically computed for such a geometry, this case first underlines to what extent the free field assumption becomes hazardous when it comes to reconstructing pressure fields at high ka ratios. From this first benchmarks, Galerkin ESM turns out to outperform CBF and iBF restricted to the free field model. For the sphere specific case, it however remains coarser than the inverse problem supplied with analytical ground truth FRFs.

Finally on experimental data, Galerkin ESM backpropagated maps provide insightful refinements on the sources directivity, especially compared to what actually used methods are likely to provide. In view of the initial motivation of the paper, i.e. scattered sound field synthesis from microphone array pressures, it appears that the approach pursued here takes on its full relevancy on this type of industrial application. Indeed, a complete set of realistic transfer functions is seldom available or at the expense of costly upstream computations, and it has been shown that Galerkin ESM provides an efficient

framework to grasp strongly directive patterns while bypassing the FRF simulation step.

ACKNOWLEDGMENTS

The authors would like to thank Thibaut Le Magueresse (from Amiral Technologies, France and formerly from MicrodB) for making experimental results possible, and for his early stage intuitions on involving equivalent sources directly in the imaging inverse problem.

Antoni, J. (**2012**). "A Bayesian approach to sound source reconstruction : Optimal basis, regularization, and focusing," Journal of the Acoustical Society of America **131**, 2873–2890, doi: 10.1121/1.3685484.

Antoni, J., Le Magueresse, T., Leclère, Q., and Simard, P. (**2019**). "Sparse acoustical holography from iterated Bayesian focusing," Journal of Sound and Vibration **446**, doi: 10.1016/j.jsv.2019.01.001.

Bai, M. R., Chen, C.-C., and Lin, J.-H. (**2011**). "On optimal retreat distance for the equivalent source method-based nearfield acoustical holography," Journal of the Acoustical Society of America **129**(3), 1407–1416, doi: 10.1121/1.3533734.

Bonnet, M. (**1999**). *Boundary integral equations methods in solids and fluids* (John Wiley and sons), pp. xx+391 pages.

Bouchet, L., Loyau, T., Hamzaoui, N., and Boisson, C. (**2000**). "Calculation of acoustic radiation using equivalent-sphere methods," Journal of the Acoustical Society of America **107**(5), 2387–2397, doi: 10.1121/1.428625.

Burton, A. J., and Miller, G. F. (**1971**). "The application of integral equation methods to the numerical solution of some exterior boundary-value problems," Proceedings of the Royal Society of London. Series A, Mathematical and Physical Sciences **323**(1553), 201–210, doi: 10.1098/rspa.1971.0097.

Chambon, J., Le Magueresse, T., Minck, O., and Antoni, J. (**2020**). "3D Beamforming for wind tunnel applications using ESM based transfer functions," Berlin Beamforming Conference .

Chen, I.-L. (**2006**). "Using the method of fundamental solutions in conjunction with the degenerate kernel in cylindrical acoustic problems," Journal of the Chinese Institute of Engineers **29**, 445–457, doi: 10.1080/02533839.2006.9671140.

Chiariotti, P. (**2019**). "Acoustic beamforming for noise source localization – reviews, methodology and applications," Mechanical Systems and Signal Processing **120**, 422–448, doi: 10.1016/j.ymssp.2018.09.019.

Duda, R. O., and Martens, W. L. (**1998**). "Range dependence of the response of a spherical head model," Journal of the Acoustical Society of America **104**, 3048–3058, doi: 10.1121/1.423886.

Dunn, M. H., and Tinetti, A. F. (**2004**). "Aeroacoustic scattering via the equivalent source method," AIAA Aerospace Sciences Meeting **10**.

Fernandez-Grande, E., Xenaki, A., and Gerstoft, P. (**2017**). "A sparse equivalent source method for near-field acoustic holography," Journal of the Acoustical Society of America **141**(1), 532–542, doi: 10.1121/1.4974047.

Golub, G. H., and Van Loan, C. F. (**1996**). *Matrix Computations (3rd Ed.)* (Johns Hopkins University Press, USA).

Hald, J. (**2020**). "A comparison of compressive equivalent source methods for distributed sources," Journal of the Acoustical Society of America **147**, 2211–2221, doi: 10.1121/10.0001073.

Jeans, R., and Mathews, I. C. (**1992**). "The wave superposition method as a robust technique for computing acoustic fields," Journal of the Acoustical Society of America **92**(2), 1156–1166, doi: 10.1121/1.404042.

Kondapalli, P. S., Shippy, D. J., and Fairweather, G. (**1992**). "Analysis of acoustic scattering in fluids and solids by the method of fundamental solutions," Journal of the Acoustical Society of America **91**(4), 1844–1854, doi: 10.1121/1.403714.

Koopmann, G. H., and Fahnline, J. B. (**1991**). "A numerical solution for the general radiation problem based on the combined methods of superposition and singular-value decomposition," Journal of the Acoustical Society of America **90**, 2808–2819, doi: 10.1121/1.401878.

Koopmann, G. H., Song, L., and Fahnline, J. B. (**1989**). "A method for computing acoustic fields based on the principle of wave superposition," Journal of the Acoustical Society of America **86**, 2433–2438, doi: 10.1121/1.404042.

Le Magueresse, T. (**2016**). "Approche unifiée multidimensionelle du problème d'identification acoustique inverse," Ph.D. thesis, LAUM & LVA.

Le Magueresse, T., Antoni, J., and Minck, O. (**2018**). "Experimental applications of Bayesian focusing in an industrial context," in *ISMA*.

Le Magueresse, T., Outrequin, A., Thivant, M., Antoni, J., and Jouvray, J.-L. (**2020**). "3D acoustical characterization of an electrical engine by Bayesian focusing," 8th Berlin Beamforming Conference .

Leblanc, A., Ing, R., and Lavie, A. (**2010**). "A wave superposition method based on monopole sources with unique solution for all wave numbers," Acta Acustica united with Acustica **96**, 125–130, doi: 10.3813/AAA.918263.

Leclère, Q., Pereira, A., Bailly, C., Antoni, J., and Picard, C. (**2017**). "A unified formalism for acoustic imaging based on microphone array measurements," International Journal of Aeroacoustics **16**, 431–456, doi: 10.1177/1475472X17718883.

Lee, S. (**2017**). "Review: The use of Equivalent Source Method in computational acoustics," Journal of Computational Acoustics **25**(01), doi: 10.1142/S0218396X16300012.

Lee, S., Brentner, K., and Morris, P. (**2011**). "Assessment of time-domain equivalent source method for acoustic scattering," AIAA Journal **49**, 1897–1906, doi: 10.2514/1.J050736.

Merino-Martínez, R., Sijtsma, P., Snellen, M., Ahlefeldt, T., Antoni, J., Bähr, C., Blacodon, D., Ernst, D., Finez, A., Funke, S., Geyer, T., Haxter, S., Herold, G., Huang, X., Humphreys, M., Leclere, Q., Malgoezar, A., Michel, U., Padois, T., Pereira, A., Picard, C., Sarradj, E., Siller, H., Simons, D., and Spehr, C. (**2019**). "A review of acoustic imaging methods using phased microphone arrays," CEAS Aeronautical Journal **10**, 197–230, doi: 10.1007/s13272-019-00383-4.

Ochmann, M. (**1995**). "The source simulation technique for acoustic radiation problems," Acta Acustica **81**, 512–527.

Pavić, G. (**2005**). "An engineering technique for the computation of sound radiation by vibrating bodies using substitute sources," Acta Acustica United With Acustica **91**, 1–16.

Pereira, A. (**2013**). "Acoustic imaging in enclosed spaces," Ph.D. thesis, INSA Lyon.

Pereira, A., Antoni, J., and Leclère, Q. (**2015**). "Empirical Bayesian regularization of the inverse acoustic problem," Applied Acoustics **97**, 11–29, doi: https://doi.org/10.1016/j.apacoust.2015.03.008.

Rokhlin, V. (**1990**). "Rapid solution of integral equations of scattering theory in two dimensions," Journal of Computational Physics **86**(2), 414–439, doi: https://doi.org/10.1016/0021-9991(90)90107-C.

Saad, Y. (**2003**). *Iterative Methods for Sparse Linear Systems*, second ed. (Society for Industrial and Applied Mathematics).

Sarkissian, A. (**2005**). "Method of superposition applied to patch near-field acoustic holography," Journal of the Acoustical Society of America **118**(2), 671–678, doi: 10.1121/1.1945470.

Valdivia, N., and Williams, E. (**2007**). "Study of the comparison of the methods of equivalent sources and boundary element methods for near-field acoustic holography," Journal of the Acoustical Society of America **120**, 3694–705, doi: 10.1121/1.2359284.

Valdivia, N. P. (**2018**). "Advanced equivalent source methodologies for near-field acoustic holography," Journal of Sound and Vibration **438**, 66–82, doi: 10.1016/j.jsv.2018.08.028.

Williams, G. (**1999**). *Fourier Acoustics: Sound Radiation and Nearfield Acoustical Holography* (Elsevier Science).

Wilton, D. T., Mathews, I. C., and Jeans, R. A. (**1993**). "A clarification of nonexistence problems with the superposition method," Journal of the Acoustical Society of America **94**(3), 1676–1680, doi: 10.1121/1.408140.